

Temperature gradients in microelectrode measurements: Relevance and solutions for studies of SOFC electrode materials



T.M. Huber*, A.K. Opitz, M. Kubicek, H. Hutter, J. Fleig

Vienna University of Technology, Institute of Chemical Technologies and Analytics, Research Division Electrochemistry, Getreidemarkt 9/CTA164, EC 1060 Wien, Austria

ARTICLE INFO

Article history:

Received 5 August 2014
Accepted 2 October 2014
Available online xxxx

Keywords:

LSM
Microelectrode
Impedance spectroscopy
Finite element
Degradation
Temperature gradient

ABSTRACT

Microelectrodes on solid electrolytes, contacted by current-collecting tips, have become increasingly important for analyzing electrochemical properties of electrode materials in solid state ionics. Samples are usually asymmetrically heated from the bottom side. It is shown experimentally, e.g. by thermovoltage measurements, impedance spectroscopy and infrared camera pictures, as well as by finite element modeling that substantial temperature gradients may arise in these experiments. Consequences in terms of data analysis are discussed and ways to alleviate the problem are described. For a complete avoidance of the temperature inhomogeneity problem, a novel symmetrically heated micro-contact set-up was built.

© 2014 Elsevier B.V. All rights reserved.

1. Introduction

Electrochemical impedance spectroscopy (EIS) is a key method in solid state electrochemistry and frequently applied not only to separate electrode and electrolyte impedance contributions but also to obtain mechanistic details of electrochemical reactions, for example in solid oxide fuel cells (SOFCs), solid oxide electrolysis cells (SOECs), and gas sensors. Electrodes optimized in terms of electrochemical performance are usually porous. However, since electrode kinetics also depends on geometrical parameters such as particle size, porosity, exact morphology and phase distribution (in composite electrodes), measurements on porous electrodes are often difficult to interpret in terms of reaction pathways and rate limiting steps. Progress has recently been made by 3D reconstruction studies to clarify geometrical details of composite electrodes [1–6] but efforts to obtain such details of porous electrodes are considerable. For an effective comparison of different materials and mechanistic studies, model electrodes were therefore successfully introduced. Two types of model electrodes are employed: macroscopically sized dense thin film electrodes and microelectrodes, which themselves may or may not consist of dense thin films.

Thin film electrodes can be deposited with defined structure on single crystalline electrolyte substrates. Often symmetrical samples with two identical electrodes are prepared, which can be investigated in a homogeneously heated furnace without problems caused by temperature gradients. However, this approach is not very flexible in

terms of electrode geometry, and analysis of three phase boundary effects requires additional micro-patterning [7–12]. Moreover, meaningful DC measurements can only be obtained when applying a reversible counter electrode or a three electrode arrangement. The latter is highly non-trivial in solid state electrochemistry due to difficulties in positioning the reference electrode [13,14]. Also microelectrodes are commonly used in the field of solid state electrochemistry and a main advantage is simply the fact that minimizing the size maximizes the polarization resistance of the studied microelectrode. Hence, compared to the much larger counter electrode, a microelectrode has an orders of magnitude higher polarization resistance. Only the influence of the measured microelectrode is therefore seen in impedance spectra [7] and the counter electrode acts as a reference electrode. This geometry thus also enables measurements of the current–voltage characteristics of single electrodes.

A simple microelectrode experiment can be realized by pressing a metal wire or an oxide “pyramid” onto a single crystal [15–18]. Such experiments have been successfully performed in homogeneously heated furnaces and again avoid inhomogeneous temperature distributions in the samples. However, the corresponding microelectrode preparation or variation is elaborated, and even more important, the geometry of the point contact is rather ill-defined or hardly controllable. Therefore, geometrically well-defined thin film microelectrodes with sizes down to 10 μm in diameter have been introduced [19]. This method combines the advantages of highly defined thin film electrodes with the advantages of microelectrodes. Mostly, films with known growth properties are deposited on single crystals and micro-structured by photolithography. A current collecting contact is established under a microscope by

* Corresponding author.

E-mail address: tobias.huber@tuwien.ac.at (T.M. Huber).

means of a contact tip. Since generally many microelectrodes, partly of different sizes and shapes, exist on a single sample, the method is highly flexible and quick in terms of obtaining reasonable statistics, for example for varying geometrical parameters. Moreover, three phase boundary (3 PB) and electrode surface are easily accessible to complementary analytical measurements.

However, to the best of the authors' knowledge such experimental set-ups are so far only realized by using asymmetrically heated hot stages [20–23]. This asymmetrical heating (from the bottom side) and cooling (by convection, radiation and the contacting tip acting as a heat sink) is known to cause temperature gradients [24]. Those can lead to measurement artifacts and inconveniences including unknown exact temperature of the measured electrode, inhomogeneous temperature distribution within one electrode, additional degradation [25] and sample polarization. These uncertainties make identification of different or changing reaction pathways [7,8,24,26–31] highly nontrivial. Additionally, temperature dependent measurements on one and the same microelectrode turn out to be difficult in such set-ups due to frequent contact loss during heating. Despite these problems, there is no study available that quantifies the local temperature inhomogeneity and analyzes its effects in electrochemical measurements in more detail.

In Ref. [24] an effective temperature (T_{spr}) of the measured electrode with diameter d_{ME} was calculated from the spreading resistance of the single crystalline electrolyte (YSZ = yttria stabilized zirconia). From the YSZ bulk (spreading) resistance R_0 and the known conductivity (σ_{ion})-temperature (T) relation with parameters E_a and σ^* , a temperature is calculated from

$$\sigma_{ion} = \frac{1}{2d_{ME}R_{bulk}} = \sigma^* \cdot e^{-\frac{E_a}{k_B T}} \quad (1)$$

according to

$$T_{spr} = \frac{E_a}{k_B \cdot \ln(2d_{ME}R_0)} \quad (2)$$

This calculated temperature, however, is only an average temperature in the electrolyte region close to the microelectrode. It does not give exact information on the electrode surface temperature and the lateral thermal gradient inside the electrode itself. Moreover, this estimation via Eq. (2) is limited to circular electrodes.

In the present contribution, we first analyze the inhomogeneous temperature distribution in electrodes on asymmetrically heated samples. Several methods are used to quantify the problem, including impedance measurements, micro-thermocouple measurements, and infrared camera visualization. Moreover, finite element calculations are employed to further analyze the temperature distribution. The influence of parameters such as temperature range, electrode size and contact tip diameter is investigated. In the second part, we introduce a novel micro-contact set-up (named MiMa). It allows combination of the advantages of symmetrically heated samples and microelectrode measurements on well-defined thin film microelectrodes with sizes down to 30 μm . The performance is demonstrated by different examples. For comparison, measurements are also conducted on a new, computer controlled, asymmetrically heated micro-contact set-up.

2. Experimental

2.1. Sample preparation

($\text{La}_{0.8}\text{Sr}_{0.2}$) MnO_3 powder from Sigma Aldrich was isostatically pressed, sintered for 12 h at 1200 °C in air and used as target for the pulsed laser deposition (PLD) of thin films. Films were deposited on polished YSZ (100) single crystals (9.5 mol% Y_2O_3 , CrysTec

GmbH, Germany) using a KrF excimer laser (248 nm, COMPex Pro 101 F, Lambda Physics, Germany). Laser beam energy was set to 400 mJ per pulse at 10 Hz pulse frequency. The deposition was performed in $4 \cdot 10^{-2}$ mbar O_2 atmosphere at substrate temperatures up to 900 °C. The temperature at the YSZ surface was monitored by a pyrometer (Heitronics KT-19.99, Germany). The film thickness (between 100 nm and 240 nm) was controlled via deposition time and measured by scanning electron microscopy (SEM, FEI Qianta 200 FEG, Netherlands) and digital holographic microscopy of microelectrodes (DHM, Lyncee Tec, Switzerland). The microstructure and film growth were analyzed by SEM and transmission electron microscopy (TEM, FEI TECNAI F20). 400 nm platinum cover layers were deposited on top of the LSM films via DC magnetron sputtering (MED 020 Coating System, BAL-TEC, Germany) of Pt (99.95% pure, OGUSSA, Austria) at room temperature. The thickness of the platinum films was measured by ex-situ calibration using a quartz crystal micro-balance as well as by SEM. Platinum films without LSM were also deposited on YSZ (100) by DC magnetron sputtering. A detailed description of the platinum thin film fabrication is given in Ref. [32]. From the films, LSM, LSM/Pt and Pt microelectrodes were prepared by photolithography and subsequent ion beam etching with 2 keV Ar ions (LSM and LSM/Pt), or chemical etching in concentrated hydro-chloric acid in the case of LSM and in nitro-hydrochloric acid for platinum.

2.2. Impedance spectroscopy

Electrochemical characterization of the Pt, LSM and LSM/Pt microelectrodes was done by means of two point impedance measurements using an Alpha-A High Resolution Dielectric Analyzer with ZG-2 interface (Novocontrol, Germany). Impedance spectra were recorded at temperatures between 280 °C and 950 °C in the frequency range of $1 \cdot 10^6$ Hz to $1 \cdot 10^{-3}$ Hz with a resolution of 5 points per frequency decade. Parameterization of the spectra was carried out by the complex nonlinear least square (CNLS) fit software Z-View2 (Scribner, USA). The equivalent circuits used to fit the experimental data are shown in Fig. 1 (CPE means constant phase element). No attempt was undertaken to interpret R_1 , R_2 , and (R_3), fitting was thus only performed to determine the DC polarization resistance of the electrode, given by the sum of $R_1 + R_2 + (R_3)$.

2.3. Optimized asymmetrically heated micro-contact stage

An improved micro-contact set-up (Fig. 2) was used for measurements with asymmetrically heated hot stage. It allows set temperatures up to 1000 °C and experiments in variable gas atmosphere with pressures from 2 bar to $5 \cdot 10^{-2}$ mbar. Moreover, a high pressure washing bottle is included to control the humidity during the measurements. Possibility of highly accurate and reliable contacting of microelectrodes is achieved by placing all moving parts for contacting inside the heated vacuum chamber. These moving parts are designed with minimum size and fabricated of stiff materials, making the set-up less prone to vibration induced decontacting of the microelectrodes. Nine computer

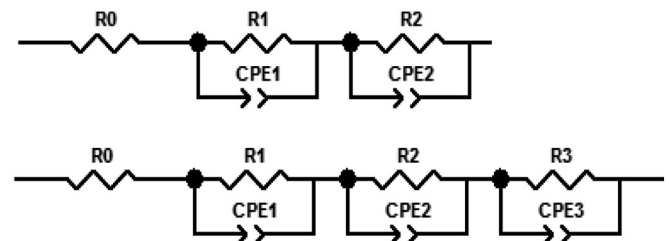


Fig. 1. Equivalent circuits used for the complex nonlinear least square fits.

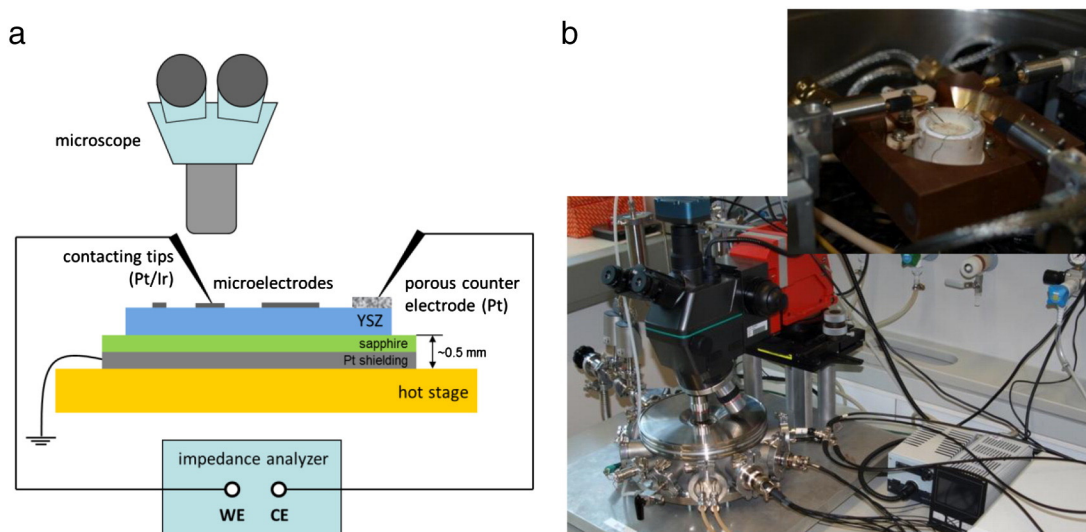


Fig. 2. (a) Sketch of the conventional micro-contact set-up with asymmetric heating. (b) Photograph of the improved set-up and view on the hot stage mounted on a cooling stage inside the vacuum chamber.

controlled piezo actuators (Agilis Newport, USA) are applied with step size of 50 nm in X- Y-, and Z-direction for positioning up to three contacting tips. Electrical contact to the measured electrodes is established under a microscope (Mitutoyo, Japan) using a USB camera. The set-up allows contacting of small structures down to the μm scale and changing the contacted electrode within seconds. The hot stage for asymmetric heating was mounted on a water cooled stage as heat protection for the piezo actuators. The whole set-up is placed on a vibration damping table.

Even though the vacuum chamber acts as Faraday cage, the hot stage inside the vacuum chamber can influence the impedance spectroscopy measurements. Stray fields can be minimized with an electrically grounded shielding plate between sample and hot stage but only at the expense of a decrease of the sample temperature compared to the set temperature. Despite all optimizations it remains difficult to perform measurements on one single microelectrode without losing electrical contact while increasing (high) temperatures: Since the contacting needle is fixed at the cold end and is not exactly perpendicular to the sample surface (to retain visibility of the electrode in the microscope), thermal expansion of all parts during temperature increase often causes disconnection of a microelectrode.

3. The temperature distribution in an asymmetrically heated sample and visualization of its consequences

3.1. Measurements of local temperature distributions and their consequences

For temperature measurements a sample set-up was chosen consisting of a 400 nm Pt film on a 0.5 mm thick YSZ single crystal. The film was micro-structured (circular microelectrodes of $\varnothing = 50\text{--}300 \mu\text{m}$) with a remaining continuous platinum film (ca. 1 mm in width) at the edges of the YSZ crystal. Two different contact tips were used, one platinum (a) and one platinum (90%)/rhodium (10%) (b). Both tips are the ends of long thin wires directly connected to type S thermocouple compensation wires. The first experiment is based on thermovoltage measurements in an asymmetrically heated micro-contact set-up. The hot stage temperature was set to 800 °C ($T_{\text{hot stage}}$) and both contacting tips were placed in a distance of several millimeters on the continuous Pt film at the sample edge (Fig. 3 (1.)). The platinum tip (a) together with the platinum film on the YSZ sample acts as negative part of a thermocouple type S, the Pt/Rh tip (b) as the positive one.

The thermovoltage measured between the two wires is determined by the exact local temperature of the Pt/Rh tip (b) on the Pt film (marked with arrow (A) in Fig. 3). The reference point of the thermocouple was at room temperature.

This measurement reveals how much the contact tip affects the local temperature by cooling. For a hot stage set temperature of 800 °C the measured thermovoltages reveal local temperatures (T_{TC}) far below this set value: For a contact tip with a tip radius of 2 μm 580 °C is found, while a blunt tip (> 10 μm radius) causes even 570 °C. Reducing convection by an additional cover plate above the sample reduces the difference to the set temperature (606 °C for 2 μm tip radius) and indicates that the local cooling is not entirely caused by the contact tip. However, this local temperature at the tip is the lowest one in the entire sample and calculations (see below) as well as a second type of “temperature measurement” show that large parts of the microelectrode and the bulk beneath the microelectrode are much closer to the set temperature.

The second estimate of the “local” temperature was obtained indirectly from a measured resistance: The impedance was measured between the microelectrode being contacted by the Pt/Rh tip and the extended Pt film counter electrode (Fig. 3 (2.)). The YSZ electrolyte resistance was extracted from the impedance spectrum and a temperature (T_{spr}) was calculated from Eq. (2) [24]. The bulk resistance of such a microelectrode experiment is largely determined by a small sample region which roughly corresponds to a hemisphere with a radius of the microelectrode diameter [33] (Fig. 3b below red area B).

Smaller electrodes lead to lower average temperatures, with values of 710 °C (740 °C) measured with 2 μm contact tip radius and $\varnothing = 50 \mu\text{m}$ (200 μm) microelectrode for 800 °C set temperature of the hot stage. For comparison, also a blunt tip with a tip radius of > 10 μm was used for impedance measurements on the same microelectrodes. Those showed much stronger cooling effects with a temperature of 660 °C for a $\varnothing = 50 \mu\text{m}$ microelectrode. Obviously, differences between sharp and blunt tips are more pronounced for T_{spr} compared to T_{TC} since the large contact area between tip and microelectrode draws more heat out of the sample.

Hindering the convective cooling by closing the vacuum chamber again decreased the difference to the set temperature by a few degrees. The cooling also strongly depends on the contacting force which presumably changes the contact area between tip and microelectrode but also heat transfer from the hot stage to the sample. Calculated

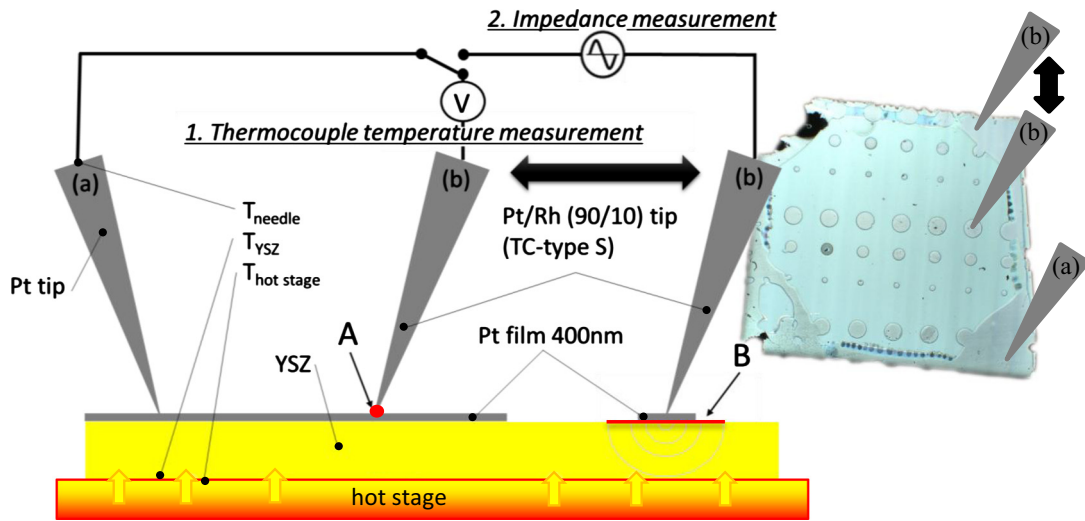


Fig. 3. Measurement of the temperature distribution for platinum microelectrodes and a continuous platinum film on YSZ, using micro-thermocouple measurements (1) and impedance spectroscopy (2). Arrow A and arrow B point on a red spot or line, thus on red area indicating the relevant region of the measurement. (For interpretation of the references to color in this figure legend, the reader is referred to the web version of this article.)

temperature values (T_{spr}) for microelectrode diameters from $\varnothing = 50 \mu\text{m}$ to $\varnothing = 200 \mu\text{m}$, measured with sharp and blunt contacting tip for open and closed cover plate, are summarized in Fig. 4a. In this diagram, also the local temperature at the contact tips (T_{TC}) is shown, measured in the micro-thermocouple experiment described above. Not surprisingly this local temperature is substantially lower than T_{spr} since it is the lowest temperature of the entire sample while T_{spr} averages over a certain bulk region.

3.2. Simulation of the local temperature distribution

Finite element calculations were performed by COMSOL© (COMSOL Group, Sweden) for a cylindrical YSZ sample, 5 mm in diameter and 0.5 mm in thickness. In the center of the top side there was a microelectrode with varying diameter (d_{ME}) from $\varnothing = 20 \mu\text{m}$ to $\varnothing = 300 \mu\text{m}$ (thickness of 200 nm) and a current collecting tip with varying contact radius from $0.5 \mu\text{m}$ to $10 \mu\text{m}$. The geometry is shown in

Fig. 5 (cylindrical electrolyte only partly visible), together with typical temperature distributions. The shape of the tip resembles that of the tips used in the experiments. A counter electrode was placed on the bottom side. Temperature and current distributions were calculated in the sample. The model also includes cooling effects by convection in air, thermal conduction in the Pt tip and radiation to the ambience. The temperature distribution in the sample was calculated by solving the equation

$$\rho C_p \frac{\partial T}{\partial t} - \nabla \cdot (k \nabla T) = Q \tag{3}$$

which includes the following material properties: density ρ ($\rho = 5680 \text{ kg} \cdot \text{m}^{-3}$ for YSZ and $\rho = 21450 \text{ kg} \cdot \text{m}^{-3}$ for Pt), the heat capacity C_p ($C_p = 0.6 \text{ J} \cdot \text{kg}^{-1} \cdot \text{K}^{-1}$ for YSZ and $C_p = 130 \text{ J} \cdot \text{kg}^{-1} \cdot \text{K}^{-1}$ for Pt), thermal conductivity k ($k = 2.5 \text{ W} \cdot \text{m}^{-1} \cdot \text{K}^{-1}$ for YSZ and $71.6 \text{ W} \cdot \text{m}^{-1} \cdot \text{K}^{-1}$ for Pt), heat source (or sink) $Q = 0$. If not mentioned otherwise, the

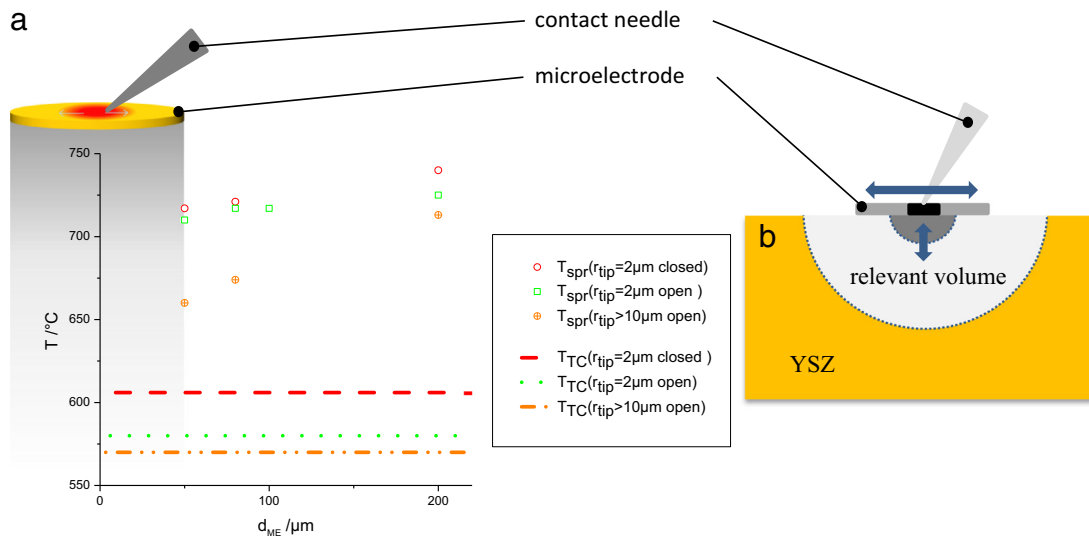


Fig. 4. (a) Temperatures determined for different Pt microelectrodes of radius r_{ME} on an asymmetrically heated sample with set temperature $T_{hot stage} = 800 \text{ }^\circ\text{C}$. Lines indicate temperatures T_{TC} measured with a micro-thermocouple. “Open” and “closed” indicate whether or not the vacuum chamber is closed by its cover plate. (b) Sketch indicating the volume relevant for T_{spr} (approximation according to Ref. [24]) and its dependence on the microelectrode size.

microelectrode is assumed to be an oxide microelectrode with ρ , C_p , and k values approximated by those of YSZ. The boundary conditions

$$-n \cdot (-k\nabla T) = h \cdot (T_{\text{amb}} - T) \quad (4)$$

describe convection of the surfaces with normal vector n . The heat transfer coefficient h depends on the dimensions of the exposed surface, air pressure and the ambient temperature T_{amb} ; it was calculated according to the model implemented in Comsol [34] for natural convection of a horizontal plate aligned upside in air of 1 atm. Radiation to ambience is described by

$$-n \cdot (-k\nabla T) = \varepsilon k_B (T_{\text{amb}}^4 - T^4) \quad (5)$$

including the surface emissivity ε , and Boltzmann's constant k_B . In all simulations the bottom side of the YSZ (T_{YSZ} in Fig. 3) was set to 800 °C, i.e. any temperature step between hot stage and sample bottom side (Fig. 3) was neglected. All other surfaces included a convection term (Eq. (4)) and thermal radiation (Eq. (5)) with surface emissivity $\varepsilon = 0.7$ for YSZ and oxide microelectrode and $\varepsilon = 0.5$ for platinum.

Typical temperature distributions are shown in Fig. 5 and reveal very strong temperature gradients close to the contact tip. Fig. 6 displays temperature distributions along the surface of the microelectrode for different tip radii of the contact needle and different microelectrode diameters. Most obvious is the very strong temperature drop by more than 200 °C directly beneath the contact tip. This result is in excellent agreement with the thermocouple measurements shown in Section 3.1. However,

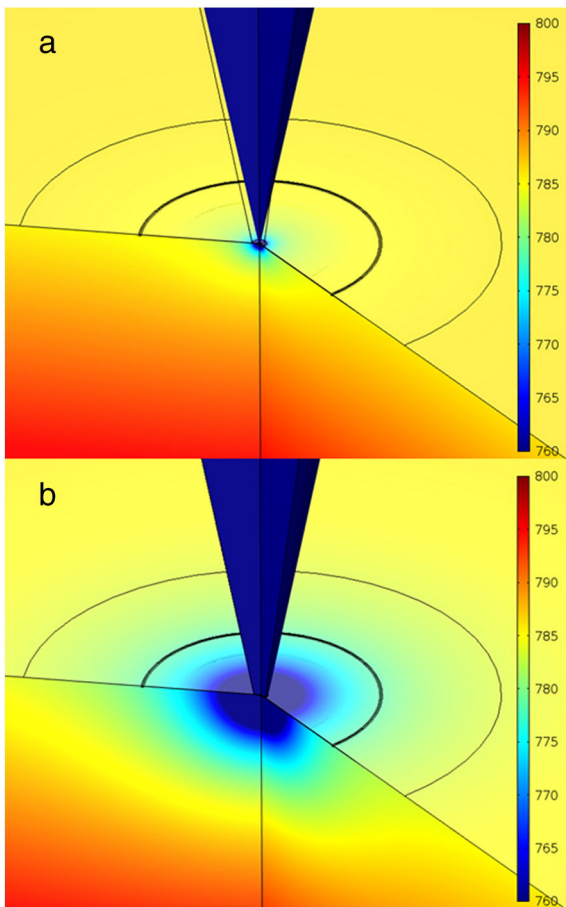


Fig. 5. 3-D picture of the temperature distribution of a $\phi = 200 \mu\text{m}$ microelectrode calculated by the finite element method, hot stage set temperature of 800 °C, contact tip radius of (a) 1 μm and (b) 9 μm , temperature range from 760 to 800 °C. The inner circle represents the $\phi = 200 \mu\text{m}$ microelectrode, the outer circle corresponds to the distance of two times the electrode diameter ($2 \cdot d_{\text{ME}} = 400 \mu\text{m}$).

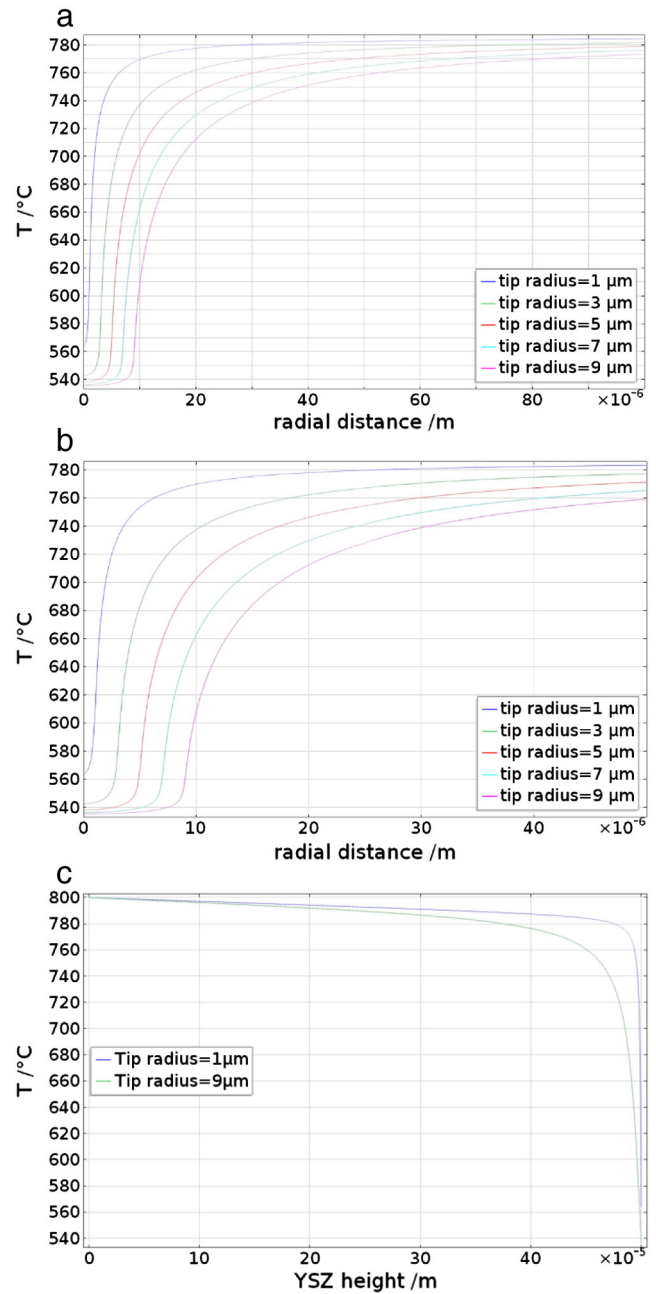


Fig. 6. Calculated temperature distribution along the YSZ microelectrode interface showing the influence of the contact tip radius for (a) a $\phi = 200 \mu\text{m}$ and (b) a $\phi = 50 \mu\text{m}$ electrode at 800 °C set temperature (T_{YSZ}). (c) Temperature distribution along the Z-axis, perpendicular to the microelectrode surface into YSZ, beneath the contact tip, for two different tip radii of 1 and 9 μm .

this does not mean that the entire microelectrode is at low temperature. Rather, the temperature sharply increases within a few μm to much higher values and large parts of the microelectrode exhibit temperature variations of “only” 10 to 30 °C. Particularly for very sharp tips most of the lateral temperature inhomogeneity can be localized to a very small region in the center of the microelectrode. Fig. 6c displays temperature distributions in Z-direction (into the YSZ beneath the contact tip, perpendicular to the microelectrode surface) for 1 and 9 μm tip radii. Also the cooling in the YSZ depth is strongly influenced by the tip radius. The fact that the surface T is lower than the set temperature of the hot stage also for sharp tips (and even without tips) is due to heat losses caused by radiation and convective cooling at the entire sample surface (see also Fig. 5 color gradient in Z-direction/in tip direction).

This calculated temperature distribution was then used to determine the local conductivity of YSZ according to Eq. (1) with $E_a = 0.767$ eV and $\sigma_0 = 157.9 \pm 16.3 \Omega^{-1} \cdot \text{cm}^{-1}$. E_a and σ_0 were experimentally obtained from impedance measurements and are valid in the temperature range from 675 to 1000 °C. For the sake of simplicity, these parameters were used for all temperatures considered here, accepting small errors (e.g. 3% error of YSZ conductivity at 550 °C). More specific, a second finite element simulation was simultaneously performed by solving

$$\text{div}(-\sigma \cdot \text{grad}(\varphi)) = 0 \quad (6)$$

which includes the temperature dependent electrical conductivity σ and the electrical potential φ . Boundary conditions were $\varphi = -1$ V at the contacting tip and $\varphi = 0$ V at the hot stage. The resulting current density distribution was used to calculate the effective YSZ bulk (spreading) resistance and then an averaged temperature was determined from Eq. (2), as in the experiment. These temperatures (T_{spr}) are plotted in Fig. 7. The cooling power of the current collecting tip and the holding clamp was estimated from temperature measurements by a thermocouple. For 800 °C hot stage set temperature a clamp temperatures of 200 °C was measured in a distance of 15 mm from the hot stage.

Despite the unavoidable temperature gradient it might be reasonable to define also a kind of “effective” temperature of the microelectrodes. The most appropriate approach, however, depends on the mechanism of the electrochemical electrode reaction. For systems with prevailing three phase boundary (3 PB) mechanism the temperature of the outer rim of the microelectrode is relevant. Fig. 7 displays how much this temperature ($T_{3\text{PB}}$) depends on tip radius and microelectrode diameter. The difference between T_{spr} and $T_{3\text{PB}}$ is not very pronounced (5.5 K for a $\varnothing = 80 \mu\text{m}$ electrode with $r_{\text{tip}} = 1 \mu\text{m}$ and 13.3 K for a $\varnothing = 200 \mu\text{m}$ electrode with $r_{\text{tip}} = 9 \mu\text{m}$, both 800 °C hot stage set temperature) with $T_{3\text{PB}}$ being always lower than T_{spr} . Therefore T_{spr} is indeed a reasonable estimate of the true 3 PB temperature. Moreover the temperature distribution is only slightly influenced by the electrode material. The simulation for a LSM microelectrode gives a slightly higher three phase boundary temperature compared to a Pt microelectrode, caused by the better thermal conduction of Pt.

For a bulk path with oxygen exchange taking place at the entire surface [19,35–37], it is more appropriate to calculate an area-weighted temperature similar to the way of determining effective temperatures from the spreading resistance. We therefore define

$$T_{2\text{PB}} = \frac{4}{d_{\text{ME}}^2} \int T(r) \cdot r \cdot 2 \cdot dr. \quad (7)$$

(It would be even more accurate to also include an Arrhenius type weighting factor in the integral. Then the result would depend on the

activation energy.) The calculated temperature $T_{2\text{PB}}$ is always lower than the 3 PB temperature (Fig. 7) and is more sensitive to the tip cooling power. The influence of the needle cooling decreases with increasing electrode diameter since the local cooling beneath the tip is almost independent of the microelectrode and its size. However, the averaged cooling effect, reflected by $T_{2\text{PB}}$, is stronger on smaller microelectrodes. Particularly for large contact tip radii and small microelectrodes T_{spr} might significantly overestimate $T_{2\text{PB}}$. Moreover, the exact value of $T_{2\text{PB}}$ is strongly influenced by the convection behavior.

All together two rules of thumb might be given. The temperature of the heavily cooled sample part beneath the contact tip is mainly determined by the hot stage set temperature and the mere fact of using a contact tip but much less by the tip radius. The size of the cooled area on the microelectrode, however, strongly depends on the contact tip size. A small tip radius (1–2 μm) only lowers the temperature in a small area while a blunt tip ($r_{\text{tip}} > 5 \mu\text{m}$) can affect a significant area, of a microelectrode and can cause considerable temperature errors at high measurement temperatures, particularly for small microelectrodes with a bulk path.

3.3. Visualizing the temperature inhomogeneity

A cathodic DC voltage of -900 mV was applied to a LSM microelectrode at 372 °C set temperature. After a time span of 200 s a steady state current could safely be assumed. Then a $^{18}\text{O}_2$ gas stream (97% isotopic enrichment, Cambridge Isotope Laboratories, UK) with $1.5 \text{ ml} \cdot \text{min}^{-1}$ was locally supplied to a contacted LSM microelectrode for 600 s by means of a quartz capillary [38]. After such a voltage driven oxygen tracer incorporation the sample was quenched on a cold metal block. Only the contacted microelectrode was removed in hydro-chloric acid. The YSZ region beneath the former LSM electrode was investigated by time-of-flight ion mass spectrometry (ToF-SIMS 5 instrument, ION-TOF GmbH, Germany). Fig. 8a and b display the ^{18}O tracer distribution and a cross-section profile in the near-surface region, with a sputter depth of ca. 3 nm in YSZ. The ^{18}O tracer is very asymmetrically distributed with maxima at both 3PBs and much higher fraction on one side of the former microelectrode.

In principle, the enhanced tracer level at the three phase boundary could reflect the dominance of a 3 PB related surface path, compared to oxygen reduction through the LSM bulk. However, under strong cathodic bias oxygen reduction on LSM microelectrodes can be expected to take place mainly via the bulk path [35]. This is confirmed by tracer measurements performed in the novel MiMa set-up (Section 4) and thus without a temperature gradient in the sample Fig. 8c and d. An almost flat concentration profile is found in the latter case. The drastic variation in ^{18}O content in Fig. 8a, b therefore visualizes the temperature gradient, caused by the contacting tip. The tip creates a local cooling

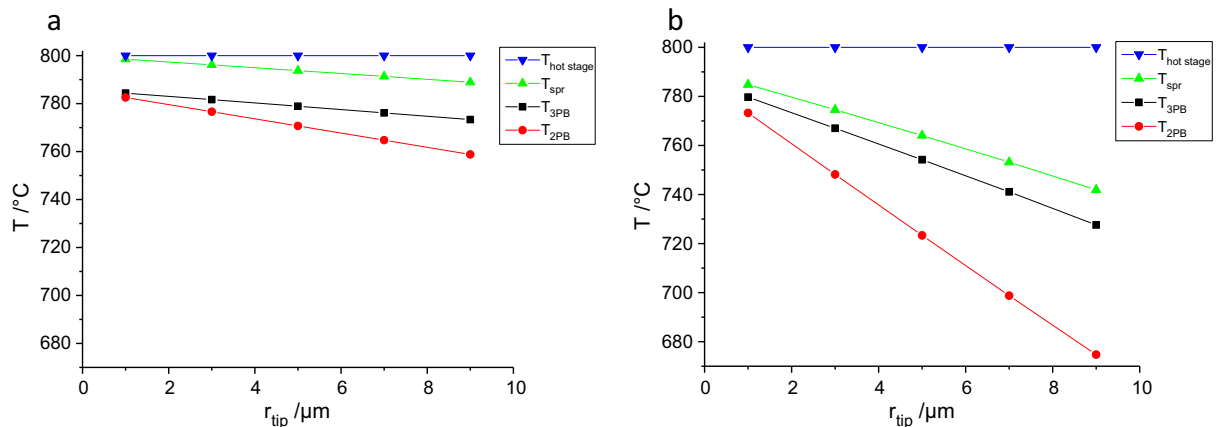


Fig. 7. Calculated temperatures for (a) $\varnothing = 200 \mu\text{m}$ and (b) $\varnothing = 50 \mu\text{m}$ LSM electrodes at 800 °C hot stage temperature contacted with different tip radii. All calculated temperatures result from simulated current distributions in the YSZ.

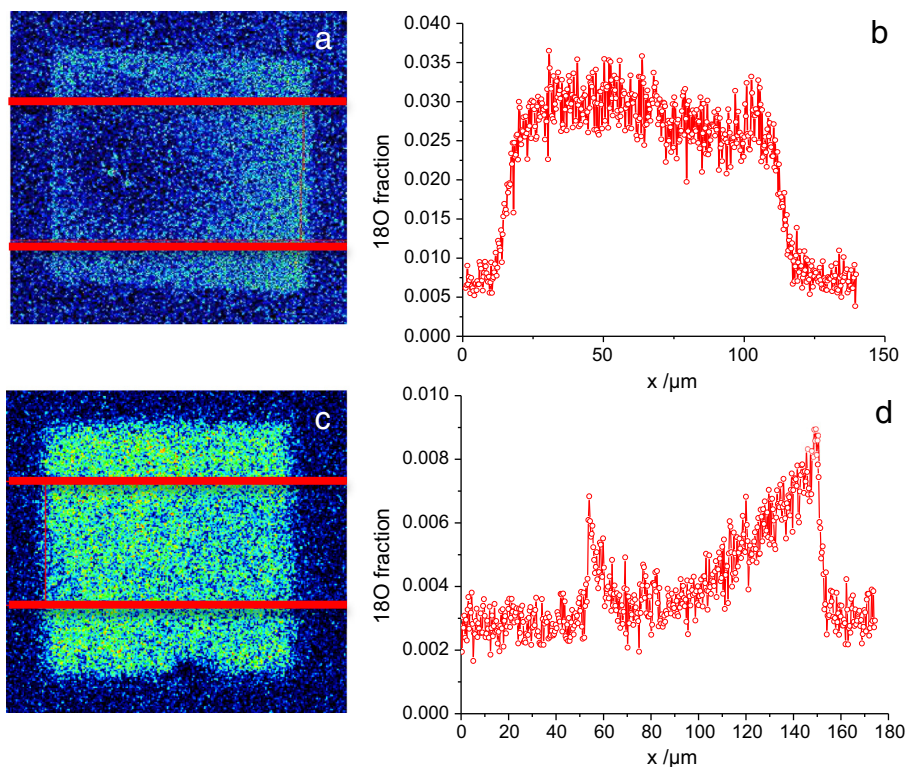


Fig. 8. (a)/(b) ^{18}O content beneath a $100 \cdot 100 \mu\text{m}^2$ LSM electrode polarized at in the conventional set-up with asymmetric heating at $T_{\text{spr}} = 372 \text{ }^\circ\text{C}$, -900 mV , $\text{ca. } 5 \cdot 10^{-8} \text{ A}$. (c)/(d) ^{18}O content beneath a $100 \cdot 100 \mu\text{m}^2$ LSM electrode measured in MiMa at $466 \text{ }^\circ\text{C}$, -900 mV , $8 \cdot 10^{-7} \text{ A}$. Red lines in (a) and (c) show the integration area for (b) and (d), respectively. Red lines in (a) and (c) indicating integration areas. (For interpretation of the references to color in this figure legend, the reader is referred to the web version of this article.)

with a lateral temperature distribution in the microelectrode. Lower temperatures decrease the thermally activated oxygen reduction and incorporation into the YSZ. The needle was located on the left part of the microelectrode and thus the oxygen incorporation was lowest close to this point. Towards the 3 PB the temperature again increases and higher tracer fractions are found, particularly on the right hand side. Bright spots at the needle contact point in the center of the dark area of Fig. 8a indicate higher ^{18}O concentration due to holes in the film. (The needle can damage the LSM film during the contacting procedure.) Further information on such experiments, also revealing true 3 PB related effects, are given in Ref. [39].

In a second experiment to visualize the temperature distribution, an infrared camera with high spatial resolution was used (Infratec, ImageIR® 9300). A color coded temperature distribution is given in Fig. 9 with one microelectrode being contacted (r.h.s.). The corresponding temperatures in cross sections of a non-contacted and a contacted microelectrode are given in Fig. 9. True temperatures may be somewhat different since materials' emission properties are not considered. At $300 \text{ }^\circ\text{C}$ hot stage set temperature the contacted $200 \mu\text{m}$ LSM electrode shows a gradient of approximately 6 K from the 3 PB to the needle. This difference seems to be small but the steepest part of the gradient is expected below the needle, and was not visible in this experiment.

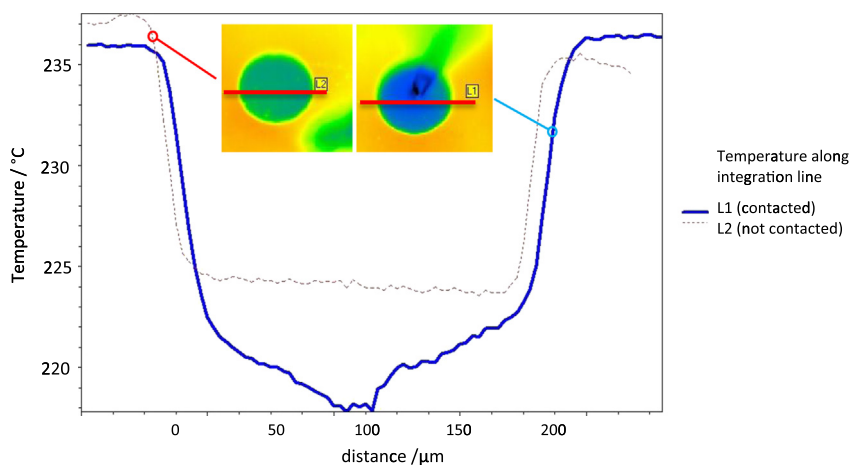


Fig. 9. Infrared camera picture of LSM microelectrodes ($\varnothing = 200 \mu\text{m}$) on YSZ, the microelectrode on the r.h.s. was contacted by a tip at hot stage set temperature of $300 \text{ }^\circ\text{C}$. Material emission properties are not included. The varying temperature distributions at the YSZ surface could be caused by infrared transition through the YSZ from the inhomogeneous Pt counter electrode on the back side of the sample. Line scans show the temperature distribution of a contacted (blue) and a not contacted (red dotted) LSM microelectrode (lines are indicated) in the infrared picture. (For interpretation of the references to color in this figure legend, the reader is referred to the web version of this article.)

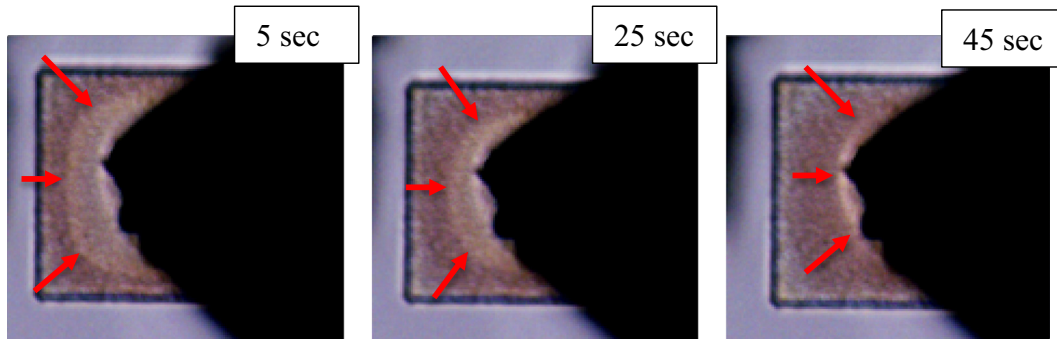


Fig. 10. 100 μm² squared LSM electrode at T_{set} = 400 °C after exposing to -3 V bias for different times (5, 25 and 45 s). Reduction starts near to the 3 PB and is slower close to the cold contacting tip. The contrast is determined by reflection rather than the true LSM color.

Indeed a finite element calculation of the expected temperature distribution for 2 μm tip radius results in a temperature decrease of 10 °C between 20 μm and 100 μm distance to the needle (center). Therefore good agreement of experiment and simulation can be concluded.

A last experiment indicating the existence of a lateral temperature profile follows. In Fig. 10 the reduction process of a LSM thin film micro-electrode, caused by high cathodic bias starts from the 3 PB region (T_{set} = 400 °C, -3 V bias). In this parameter regime (bias, temperature) oxygen reduction takes place via a bulk path [35,39] and from this one might expect a homogeneous discoloration (reduction) upon strong cathodic bias. However, discoloration in Fig. 10 is faster near the 3 PB and

becomes slower towards the contact tip which is in good agreement with the temperature decrease due to local cooling found in measurements and finite element temperature calculations.

4. Novel symmetrically heated micro-contact stage “MiMa”

4.1. Experimental realization

In order to perform microelectrode measurements in a homogeneously heated surrounding, a novel micro-contact set-up was designed (Fig. 11). In the following it is named “MiMa”, which reflects the fact that

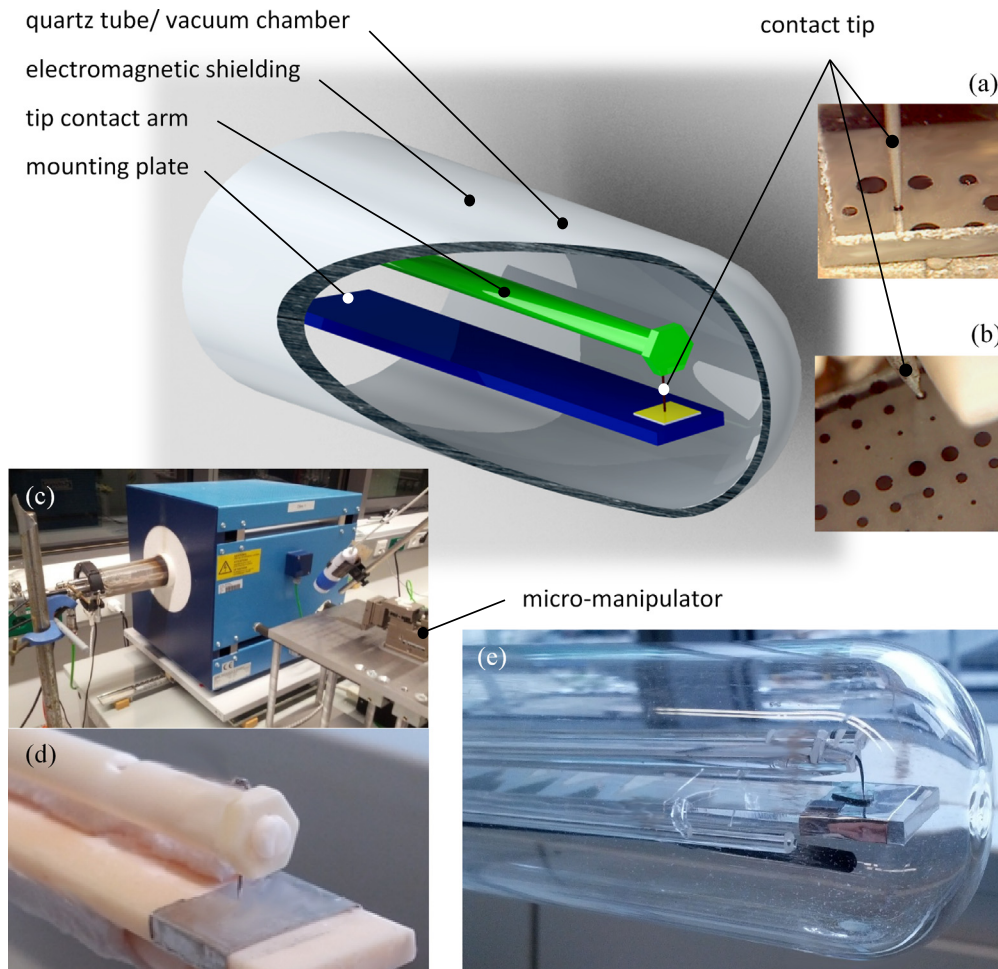


Fig. 11. 3D sketch of the tip contact arm, mounting plate and quartz tube of the symmetrically heated micro-contact set-up MiMa. Small pictures (a) & (b) show contacted microelectrodes before the tube furnace is moved over the sample. (c) Whole measurement set-up with contacting device. (d) Tip contact arm with Pt/Ir contacting tip on mounting plate with platinum foil (without sample). (e) MiMa fabricated from quartz in quartz tube with contacted sample.

microelectrodes (Mi) can be measured in a set-up usually employed for macroscopic (Ma) electrodes. Samples are essentially the same as for asymmetrically heated microelectrode measurements with microelectrodes on one side of a solid electrolyte (here YSZ single crystal) and a counter electrode on the other side (here porous platinum). The main difference to earlier microelectrode measurements in homogeneously heated set-ups [15] is the fact that in MiMa the contact tip is not used as micro-contact/microelectrode but rather only to contact well-defined thin film microelectrodes already deposited on the electrolyte.

The vacuum chamber consists of stainless steel and quartz parts. All inner parts in the heated chamber are fabricated of platinum and corundum or quartz. A corundum tube is mounted on an expansion bearing near the cold end of the vacuum tube and acts as a tip contact arm. A Pt/Ir tip is fixed on the other side of the corundum tube with a corundum screw. The contact between the microelectrode and the Pt/Ir tip is established under a microscope with a micro-manipulator outside of the heated area (Fig. 11a, b). For this purpose a micro-manipulator is moved to lift-up the tip contact arm with a blade. After the needle is aligned to the center of the selected microelectrode the tip contact arm is lowered. As soon as contact is established, blade and micro-manipulator are removed, a tube furnace is moved over the sample and the vacuum chamber is closed. A properly contacted microelectrode can now be measured from room temperature up to 1100 °C and from $1 \cdot 10^{-2}$ mbar up to 2 bar in different gas atmospheres without losing contact. The temperature is monitored with a thermocouple type S or type K positioned next to the sample. The oxygen partial pressure can be monitored with a lambda sensor (MicroPoas Setnag, France).

4.2. Reproducibility and measurement stability of microelectrode measurements in MiMa

The stability and high flexibility of MiMa microelectrode measurements in terms of temperature variations are demonstrated by an impedance measurement series on a LSM microelectrode ($d_{ME} = 300 \mu\text{m}$).

Several temperature sweeps between 560 and 860 °C and a measurement time of more than 300 h on one and the same microelectrode did not cause significant changes of the polarization resistance R_{tot} (Fig. 12). R_{tot} was obtained from the measured impedance spectra by fits to the equivalent circuit of Fig. 1, see Section 2.2. It should again be emphasized that such temperature cycles are not possible in the asymmetrically heated set-up presented in Section 2 due to frequent loss of contact during heating and destruction of the microelectrode by several contacting procedures.

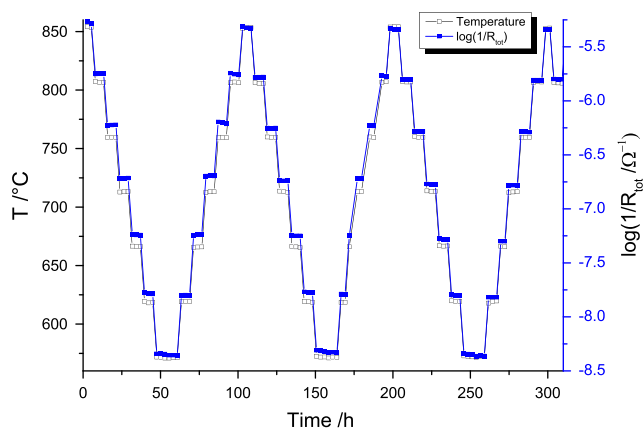


Fig. 12. Temperature and electrode polarization resistance (R_{tot}) variation of a $\varnothing = 300 \mu\text{m}$ LSM microelectrode for a long time measurement (> 300 h).

4.3. Comparison between asymmetrically and symmetrically (MiMa) heated set-up for bulk path kinetics

In a second experiment, one and the same square LSM electrode ($145 \mu\text{m}$ edge length) was analyzed by impedance spectroscopy at different temperatures in both set-ups. The series in MiMa was obtained after a single contacting procedure while in the asymmetrically heated set-up a careful contacting and de-contacting had to be performed for each temperature to avoid microelectrode damage. In a pseudo-Arrhenius plot (Fig. 13), the electrode polarization resistance is plotted versus the logarithm of the inverse high frequency off-set R_0 obtained from fits to the circuits in Fig. 1. In the case of circular microelectrodes, the YSZ bulk resistance is analytically given by Eq. (1), at least in the semi-infinite case. Here, however, rather large square microelectrodes were employed and the numerical factor relating R_0 and σ_{ion} is unknown. Hence, we use $\log(1/R_0)$, which is still proportional to a nominal T_{spr} , as X-axis in order to compare results from the two set-ups. The resistance measured in MiMa shows a change of the slope from low to high temperatures, indicating a reaction mechanism change from surface to bulk path [40]. The same is true for the measurement in the asymmetrically heated contact stage, but there the resistance decreases stronger towards higher temperatures.

This stronger change in slope is most probably a systematic error of the asymmetrically heated micro-contact set-up and related to the thermovoltage resulting from temperature gradients in the sample. For a Pt/YSZ/Pt system a thermoelectric power of $0.486 \text{ mV} \cdot \text{K}^{-1}$ was reported [41,42]. Thermovoltages of several 10 mV, often measured in our asymmetrically heated micro-contact set-ups, are in good agreement with this value. The additional thermovoltage causes a shift of the electrode reaction out of equilibrium and changes the polarization resistance R_{tot} of an impedance experiment. For LSM thin film electrodes (and many other materials) R_{tot} becomes smaller upon bias, and thus is in accordance with the result in Fig. 13. This thermovoltage induced resistance change becomes stronger towards high temperatures since the temperature gradient also increases. Complete absence of a difference between MiMa measurements and the experiment in the asymmetrically heated set-up case at lower temperatures might be caused by the fact that here the three phase boundary becomes relevant for LSM microelectrodes [40], see also Section 4.4. In general, details of the contacting procedure may affect the local temperatures and thus thermovoltages may vary significantly. Therefore different electrode resistances can easily be found for microelectrode studies in asymmetrically heated set-ups, despite nominally identical measurement conditions.

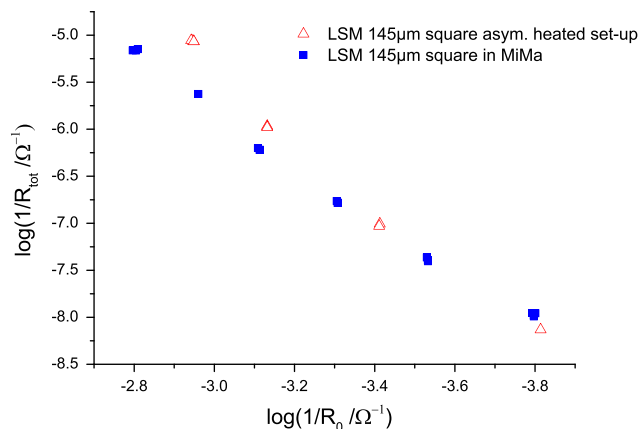


Fig. 13. $\log 1/R_{tot}$ vs. $\log 1/R_0$ from a $145 \mu\text{m}$ squared LSM microelectrode measured in MiMa and in the asymmetrically heated set-up (impedance spectra are shown in Fig. 14), temperature range is approximately 550 °C (at $\log 1/R_0 = -3.8$) to 850 °C (at $\log 1/R_0 = -2.8$).

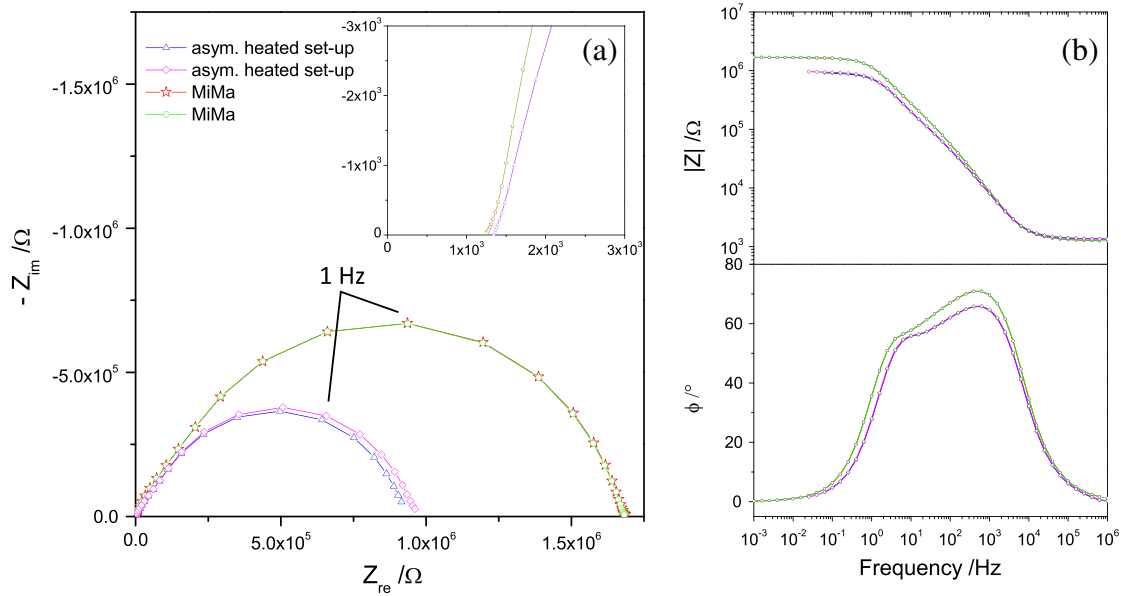


Fig. 14. Impedance spectra in Nyquist (a) and Bode plot (b) of exactly the same 145 μm squared LSM microelectrode measured in MiMa and in the asymmetrically heated set-up at 758 °C electrode and 900 °C hot stage set temperature, respectively. (Polarization resistances are plotted in Fig. 13.)

The shape of the impedance spectra (Fig. 14) measured in both set-ups shows only minor differences. However, it was reproducibly found that measurements obtained for an asymmetrically heated micro-contact set-up exhibit stronger irreversible changes. Already after 4 min the spectra were different, while data obtained in MiMa show no observable change after 25 min, both displayed in Fig. 14. This could also be related to the much stronger degradation of Pt microelectrodes found in a conventional asymmetrically heated set-up, compared to annealing with homogeneous temperature [25]. Exact reasons are not known yet, but a certain role of the temperature gradient is highly probable. Degradation might be driven by gradients in chemical potential which may not only be caused by different oxygen partial pressures, but also by voltages or temperature gradients which again lead to (thermo-)voltages. This first example revealed that both set-ups lead to the same qualitative conclusion in terms of a mechanism change but the asymmetrically heated experiment might be less reliable on a quantitative level.

A second example shows that in other cases also quantitative information fit together: It was already reported in an earlier publication that platinum microelectrodes reduce oxygen via a bulk path below 450 °C [32]. Reconsidering this experimental regime shows that no difference can be found when comparing measurements performed in MiMa and in an asymmetrically heated micro-contact set-up (Fig. 15). Here we most probably have less thermovoltage effects due to smaller measurement temperature and thereby less temperature gradients, and the determination of the exact electrode temperature is also less critical due to the low activation energy in this regime. The large spreading of data points is due to fitting inaccuracies caused by the high polarization resistance of platinum microelectrodes at these temperatures. The fitting approach is explained in Ref. [32].

4.4. Comparison between asymmetrically and symmetrically (MiMa) heated set-up for 3 PB path

One and the same LSM/Pt finger-shaped microelectrode with a large 3 PB length (Fig. 16c) was investigated in the asymmetrically heated set-up and in MiMa. In both cases a Pt/Ir needle was used to electrically contact the LSM/Pt microelectrode. The Pt capping layer on the LSM blocks large parts of the oxygen reduction via a bulk path [40,43]. The set temperatures of the temperature control units were adjusted to reach almost the same electrolyte resistance R_0 in both set-ups, see

inset in Fig. 16. When interpreting the same R_0 as an indication of the same average YSZ temperature beneath the microelectrode, the two measurements should lead to very similar results.

In contrast to the MiMa set-up, spectra measured subsequently in the asymmetrically heated micro-contact set-up slightly drift (Fig. 16), as already found for pure LSM microelectrodes (Fig. 14). Slight differences of the spectra shapes are visible in Fig. 16 and quantified by fitting the spectra to three serial R-CPE elements, see Fig. 1 bottom. The fit results are given in Table 1, including the ratios of the fit parameters for MiMa and the asymmetrically heated microelectrode measurements. Some differences are found but should not be over-interpreted since the total polarization resistance R_{tot} is very similar in both cases. This is also in line with similar measurements performed on circular Pt microelectrodes. There the 3 PB-related path is relevant in the temperature range from 450 to >800 °C [24]. The data obtained in MiMa and in an asymmetrically heated set-up show the same slope in an

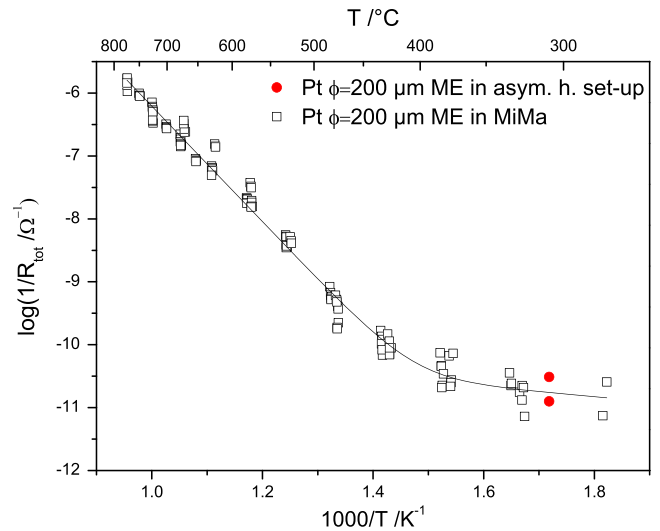


Fig. 15. Arrhenius plot of the electrode polarization resistance for $\phi = 200 \mu\text{m}$ platinum microelectrodes measured in MiMa and in the asymmetrically heated micro-contact set-up.

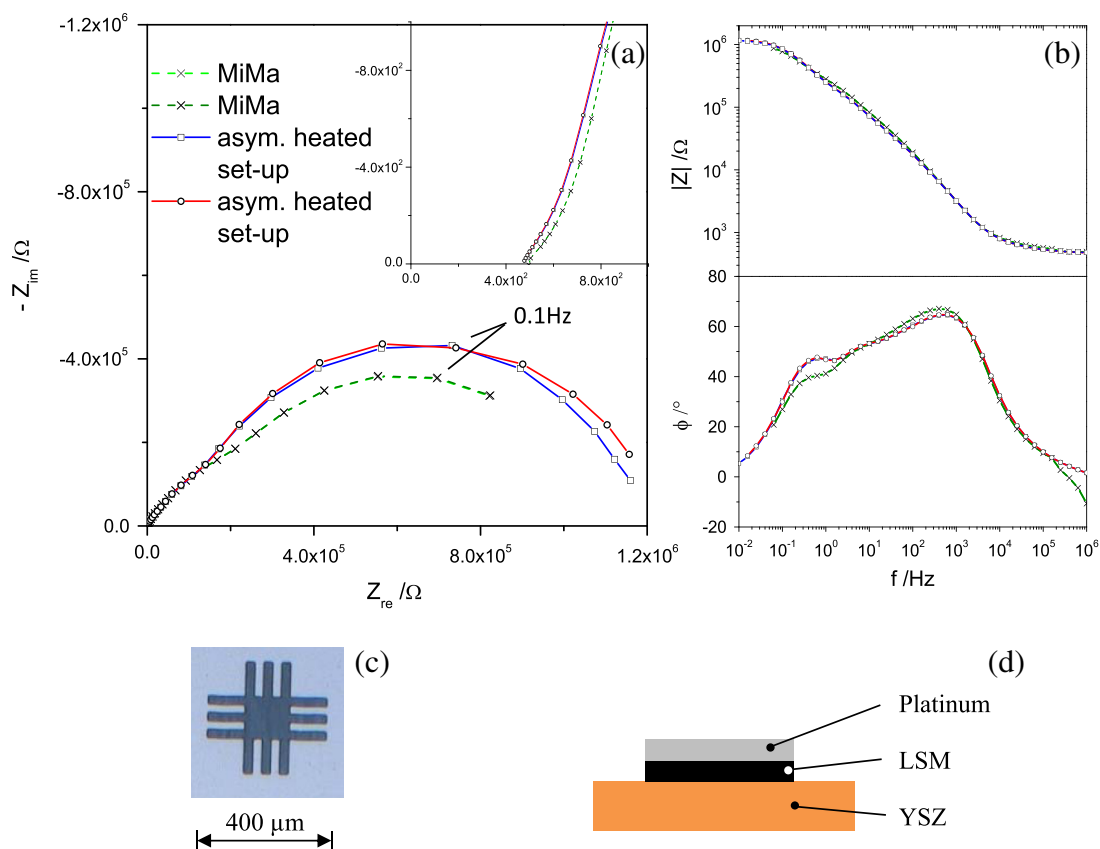


Fig. 16. Impedance spectra of a LSM microelectrode covered with Pt at 730 °C (T_{spr}) in the asymmetrically heated set-up in a Nyquist plot (a) and Bode plot (b) measured in MiMa and in the asymmetrically heated set-up. Two subsequent measurements are shown in each set-up. (c) Photograph of the LSM/Pt microelectrode and (d) sketch of the cross section.

Arrhenius plot (Fig. 17). Slight differences of absolute values might simply be due to an inaccurate temperature calculation for measurements in the asymmetrically heated set-up.

Both experiments on LSM/Pt and Pt, and also the low temperature data in Fig. 13 (LSM), show that temperature gradients have only minor impact on the results obtained for the 3 PB related surface path. The finite element simulations showed that temperatures at 3PBs are much closer to the temperature of the counter electrode (T_{YSZ}) than the tip contacts. Thermovoltages, on the other hand, represent the temperature differences at the contact tip. Those only transfer to a high driving force for a DC driven electrochemical reaction at locations with similarly large deviations from T_{YSZ} . This is not the case for 3PBs but indeed partly true for bulk path-type reactions taking place along the entire electrode surface. Accordingly, neither Pt electrodes at higher temperatures nor LSM/Pt electrodes (all temperatures) are much affected since they are determined by 3 PB kinetics. LSM at lower temperatures also exhibits a 3 PB surface path and is not prone to thermovoltage problems as well. (At lower temperature thermovoltages are less pronounced, anyway.) Only LSM at high temperatures with its predominant bulk path is severely influenced by the thermovoltages.

5. Conclusion

Conventional micro-contact set-ups with asymmetric heating can cause measurement inconveniences and measurement errors. In particular, local cooling by the current collecting tip leads to lateral temperature gradients. Those gradients were quantified and visualized by several tools such as micro-thermocouple measurements, infrared camera pictures, LSM reduction kinetics, or tracer incorporation kinetics. Finite element calculations of temperature distributions are in good agreement with experiments and show that current collecting tips induce a strong temperature decrease at the contacting point (ca. 200 K for 800 °C set temperature). The maximum temperature reduction found beneath the contact tip can mainly be influenced by preventing convection but not by the tip radius. However, temperature gradients are rather sharp and often large parts of the microelectrode are much less affected by the local temperature decrease, provided sharp contact tips and sufficiently large microelectrodes are used. The temperature estimated from the measured YSZ (spreading) resistance is in reasonable agreement with the temperature at the 3 PB but may severely overestimate the temperature of inner parts of the microelectrode. Thermovoltages of several 10 mV

Table 1

Fit results from the spectra in Fig. 16 using the equivalent circuit in Fig. 1, bottom, capacitances are calculated from CPE elements after [44].

	R_0/Ω	R_1/Ω	R_2/Ω	R_3/Ω	C_1/F	C_2/F	C_3/F
MiMa	5.41E + 02	9.31E + 03	2.37E + 05	8.04E + 05	2.70E - 07	3.30E - 07	1.64E - 06
MiMa	5.41E + 02	9.34E + 03	2.38E + 05	8.05E + 05	2.70E - 07	3.30E - 07	1.64E - 06
Asym. heated set-up	4.93E + 02	5.55E + 03	1.54E + 05	1.02E + 06	2.91E - 07	3.63E - 07	1.29E - 06
Asym. heated set-up	4.91E + 02	4.89E + 03	1.50E + 05	1.06E + 06	2.96E - 07	3.52E - 07	1.27E - 06
Ratio MiMa/Asym. h.	1.09	1.79	1.56	0.77	0.92	0.92	1.28

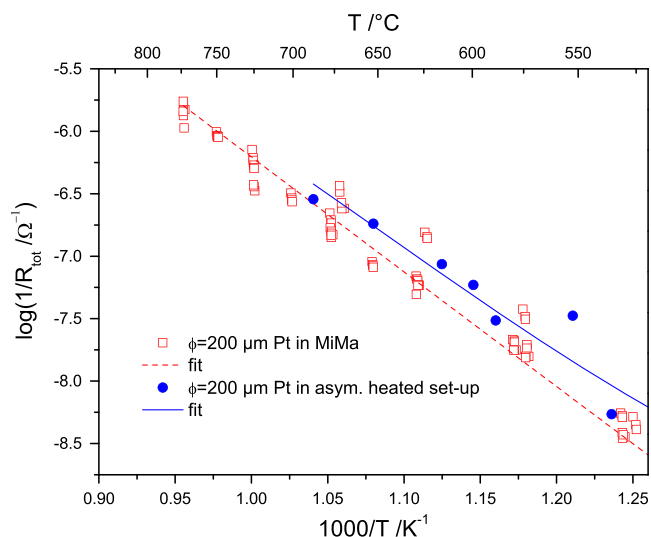


Fig. 17. Arrhenius plot of the electrode polarization resistance for $\phi = 200 \mu\text{m}$ platinum microelectrodes measured in MiMa and in the asymmetrically heated micro-contact set-up.

may arise and can cause an unintended bias load and DC current which may modify measured polarization resistances. This was indeed found for LSM microelectrodes at high temperatures with predominant bulk path. Electrodes governed by a 3 PB surface path (LSM/Pt, Pt) are much less influenced by thermovoltages, since those reflect the strongest possible temperature decrease near the contact tip. Thermally induced electrochemical driving force are much less pronounced at 3PBs. In general measurement errors caused by temperature gradients in asymmetrically heated micro-contact set-ups can be reduced by using thin sharp needles with little thermal conduction, avoidance of convection above the measured sample and choosing low measurement temperatures. Moreover, large microelectrodes exhibit less relevance of local cooling effects by the contacting tip.

For avoiding several problems occurring with set-ups using asymmetrical heating of the sample, a novel micro-contact set-up (MiMa), based on a tube furnace, was constructed. Owing to its symmetrical heating it eliminates all detrimental effects associated with temperature gradients within the sample. Moreover, it allows longtime measurements and temperature cycles. Experiments on LSM and platinum microelectrodes showed that it is possible to analyze a single microelectrode from room temperature up to $1000 \text{ }^\circ\text{C}$ without losing contact. Microelectrodes were reproducibly measured over weeks from 300 to $950 \text{ }^\circ\text{C}$ without irreversible degradation effects.

Acknowledgments

We gratefully acknowledge Elisabeth Eitenberger for SEM measurements. This work was financially supported by the Austrian Science Fund (FWF), Projects P21960-N17 and W1243-N16.

References

- [1] B. R uger, J. Joos, A. Weber, T. Carraro, E. Ivers-Tiff e, ECS Trans. 25 (2) (2009) 1211.
- [2] J.R. Wilson, W. Kobsiriphat, R. Mendoza, H.-Y. Chen, J.M. Hiller, D.J. Miller, K. Thornton, P.W. Voorhees, S.B. Adler, S.A. Barnett, Nat. Mater. 5 (7) (2006) 541.
- [3] J.R. Wilson, A.T. Duong, M. Gameiro, H.-Y. Chen, K. Thornton, D.R. Mumm, S.A. Barnett, Electrochem. Commun. 11 (5) (2009) 1052.
- [4] P.R. Shearing, J. Golbert, R.J. Chater, N.P. Brandon, Chem. Eng. Sci. 64 (17) (2009) 3928.
- [5] Z. Jiao, N. Shikazono, N. Kasagi, J. Electrochem. Soc. 159 (3) (2012) B285.
- [6] J.R. Izzo, A.S. Joshi, K.N. Grew, W.K.S. Chiu, A. Tkachuk, S.H. Wang, W. Yun, J. Electrochem. Soc. 155 (5) (2008) B504.
- [7] J. Fleig, F.S. Baumann, V. Brichzin, H.R. Kim, J. Jamnik, G. Cristiani, H.U. Habermeier, J. Maier, Fuel Cells 6 (3–4) (2006) 284.
- [8] J. Fleig, Advances in Electrochemical Science and Engineering, 8, Wiley-VCH Verlag GmbH & Co. KGaA, 2003, pp. 1–87.
- [9] M.W. Breiter, K. Leeb, G. Fafilek, J. Electroanal. Chem. 434 (1–2) (1997) 129.
- [10] A. Bieberle, L.P. Meier, L.J. Gauckler, J. Electrochem. Soc. 148 (6) (2001) A646.
- [11] M.V. Rao, J. Fleig, M. Zinkevich, F. Aldinger, Solid State Ionics 181 (25–26) (2010) 1170.
- [12] R. Radhakrishnan, A.V. Virkar, S.C. Singhal, J. Electrochem. Soc. 152 (1) (2005) A210.
- [13] S.B. Adler, B.T. Henderson, M.A. Wilson, D.M. Taylor, R.E. Richards, Solid State Ionics 134 (1–2) (2000) 35.
- [14] G. Hsieh, T.O. Mason, E.J. Garboczi, L.R. Pederson, Solid State Ionics 96 (3–4) (1997) 153.
- [15] T. Jacobsen, L. Bay, Electrochim. Acta 47 (13–14) (2002) 2177.
- [16] J. Nielsen, T. Jacobsen, Solid State Ionics 178 (33–34) (2008) 1769.
- [17] W. Zipprich, H.D. Wiemh ofer, Solid State Ionics 135 (1–4) (2000) 699.
- [18] D.S. Tsvetkov, V.V. Sereda, A.Y. Zuev, Solid State Ionics 192 (1) (2011) 215.
- [19] V. Brichzin, J. Fleig, H.U. Habermeier, J. Maier, Electrochem. Solid-State Lett. 3 (9) (2000) 403.
- [20] G.J. Ia O', Y. Shao-Horn, J. Electrochem. Soc. 156 (7) (2009) B816.
- [21] F.S. Baumann, J. Maier, J. Fleig, Solid State Ionics 179 (21–26) (2008) 1198.
- [22] L. Wang, R. Merkle, J. Maier, J. Electrochem. Soc. 157 (12) (2010) B1802.
- [23] W. Jung, H.L. Tuller, J. Electrochem. Soc. 155 (11) (2008) B1194.
- [24] A.K. Opitz, J. Fleig, Solid State Ionics 181 (15–16) (2010) 684.
- [25] M.P. H rlein, A.K. Opitz, J. Fleig, Solid State Ionics 247–248 (2013) 56.
- [26] L. Wang, R. Merkle, G. Cristiani, B. Stuhlhofer, H.-U. Habermeier, J. Maier, ECS Trans. 13 (26) (2008) 85.
- [27] S. Rodewald, J. Fleig, J. Maier, J. Am. Ceram. Soc. 84 (3) (2001) 521.
- [28] G.J. Ia O', B. Yildiz, S. McEuen, Y. Shao-Horn, J. Electrochem. Soc. 154 (4) (2007) B427.
- [29] J. Nielsen, T. Jacobsen, Solid State Ionics 178 (13–14) (2007) 1001.
- [30] T. Ryll, J.L.M. Rupp, A. Bieberle-Hutter, H. Galinski, L.J. Gauckler, Scr. Mater. 65 (2) (2011) 84.
- [31] J. Fleig, H.L. Tuller, J. Maier, Solid State Ionics 174 (1–4) (2004) 261.
- [32] A.K. Opitz, A. Lutz, M. Kubicek, F. Kubel, H. Hutter, J. Fleig, Electrochim. Acta 56 (27) (2011) 9727.
- [33] J. Fleig, J. Maier, Solid State Ionics 85 (1–4) (1996) 17.
- [34] F.P. Incropera, D.P. DeWitt, Fundamentals of Heat and Mass Transfer, 5th ed. John Wiley & Sons, 2002.
- [35] V. Brichzin, J. Fleig, H.U. Habermeier, G. Cristiani, J. Maier, Solid State Ionics 152–153 (2002) 499.
- [36] T. Ioroi, T. Hara, Y. Uchimoto, Z. Ogumi, Z. Takehara, J. Electrochem. Soc. 144 (4) (1997) 1362.
- [37] A. Endo, M. Ihara, H. Komiyama, K. Yamada, Solid State Ionics 86–88 (Part 2) (1996) 1191.
- [38] A.K. Opitz, A. Schintlmeister, H. Hutter, J. Fleig, Phys. Chem. Chem. Phys. 12 (39) (2010) 12734.
- [39] A.K. Opitz, M. Kubicek, S. Huber, T. Huber, G. Holzlechner, H. Hutter, J. Fleig, J. Mater. Res. 28 (16) (2013) 2085.
- [40] T.M. Huber, A.K. Opitz, M. Kubicek and J. Fleig, submitted for publication.
- [41] E.O. Ahlgren, F.W. Poulsen, Solid State Ionics 82 (3–4) (1995) 193.
- [42] E. Ahlgren, F. Willy Poulsen, Solid State Ionics 70–71 (Part 1) (1994) 528.
- [43] T.M. Huber, A.K. Opitz and J. Fleig, Solid State Ionics submitted.
- [44] J. Fleig, Solid State Ionics 150 (1–2) (2002) 181.